J. Iron Steel Res. Int.
https://doi.org/10.1007/s42243-023-01098-x

ORIGINAL PAPER

Mechanical performance of 22SiMn2TiB steel welded with low-transformation-temperature filler wire and stainless steel filler wire

Zi-dong Lin[1,2,3] · Kai-jie Song[1,2] · Zhen Sun[2] · Zi-qian Zhu[1,2] · Xue-feng Zhao[1,2] · Constantinos Goulas[3] · Wei Ya[4] · Xing-hua Yu[1,2]

Received: 24 March 2023 / Revised: 5 June 2023 / Accepted: 14 June 2023

Abstract
TX-80 low-transformation-temperature (LTT) welding wire was used to replace the traditional ER 307Si welding wire to realize the connection of 22SiMn2TiB armor steel in manual overlay welding. The previously existing issues, such as welding cracks, large welding deformation, and severe welding residual stress, were solved to ensure good strength and ductility requirements. In particular, with the same welding conditions, TX-80 LTT wire eliminates welding cracks. It reduces the welding deformation no matter the base pretreatment of pre-setting angle or no pre-setting angle. By comparison, it was found that the microstructure at the TX-80 weld is mainly composed of martensite and a small amount of retained austenite. In contrast, the microstructure of the ER 307Si weld consists of a large amount of austenite and a small amount of skeleton-like ferrite. The variation trend of residual stress and microhardness from the weld to the base were investigated and compared with the mechanical properties of base materials. The TX-80 and the ER 307Si tensile samples elongation is 6.76% and 6.01%, while the ultimate tensile strengths are 877 and 667 MPa, respectively. The average impact toughness at room temperature of the ER 307Si weld is 143.9 J/cm^2, much higher than that of the TX-80 weld, which is only 36.7 J/cm^2. The relationship between impact and tensile properties with microstructure species and distribution was established. In addition, the fracture surface of the tensile and the impact samples was observed and analyzed. Deeper dimples, fewer pores, larger radiation zone, and shear lips of TX-80 samples indicate better tensile ductility and worse impact toughness than those of ER 307Si weld.

Keywords Low-transformation-temperature material · 22SiMn2TiB steel · Welding deformation · Residual stress · Martensitic transformation · Mechanical property

1 Introduction

Steels are the most commonly used alloy in many fields, such as structural applications in aerospace [1], construction [2], and maritime [3, 4]. Low-carbon high-strength steel (LCHS) is lightweight and has good formability and weldability. Therefore, LCHS has become potential material for weight reduction and performance improvement in the armored vehicles industry [5]. Their application indicates that LCHS can effectively reduce the cross-sectional size of components and the structure's weight, leading to a decrease in energy consumption and enhanced mobility of armored vehicles, such as improving the protection ability [6]. 22SiMn2TiB Steel, as one type of LCHS, is composed of martensite and bainite. In the past few years, it has attracted much attention in armored troop carrier vehicles because of its comprehensive mechanical properties, including high strength and hardness, high-temperature resistance, and excellent formability. However, it has been regarded as a suitable candidate for more and more lightweight applications [7–9] today, which is motivating us to carry out the current study.

Zi-dong Lin and Kai-jie Song contributed equally to this work.

✉ Xing-hua Yu
xyu@bit.edu.cn

1 School of Materials Science and Engineering, Beijing Institute of Technology, Beijing 100081, China

2 Beijing Institute of Technology Chongqing Innovation Center, Chongqing 401120, China

3 Department of Design Production and Management, Faculty of Engineering Technology, University of Twente, Enschede 7500 AE, The Netherlands

4 Rotterdam Additive Manufacture Fieldlab (RAMLAB), Rotterdam 3089 JW, The Netherlands

Published online: 30 October 2023

Although LCHS has good weldability due to low carbon content, it is still challenging to mitigate cracking. For example, Beidokhti et al. [10] investigated the alloying elements and microstructure on the susceptibility of the welded high-strength low-alloyed (HSLA) steel to hydrogen-induced cracking and sulfide stress cracking. It was found that under the composition of 1.40 wt.% Mn–0.08 wt.% Ti and 1.92 wt.% Mn–0.02 wt.% Ti, the weld containing a high percentage of acicular ferrite and reasonable distribution of titanium carbonitrides yielded the best performance in sour services. Papaefthymiou et al. [11] found that hard and brittle (Ti, V)N inclusions and slag particles acted as the crack driving force and implied an overall detrimental effect on the fatigue strength and lifetime of the high-resistance structural steel component. Besides, the thermal effect during welding worsens the steel base near the weld region, such as heat-affected zone (HAZ), which is easy to produce cracks during the cooling process. Yu et al. [12] observed hardening and softening behavior in the different HAZ regions of BA-160. Steel was explained by the relative strength contributions from lath martensite morphology and Cu precipitates. This phenomenon also observed by Mohandas et al. [13] further indicated that steel with a high carbon equivalent exhibited maximum softening. As mentioned earlier, 22SiMn2TiB steel as LCHS has been studied for many years with different welding techniques, such as arc welding [14], laser welding [15], and electron beam welding (EBW) [16]. Xu et al. [7] investigated the softening behavior of 22SiMn2TiB steel welded by EBW using experimental and numerical simulation methods. The results indicated that the microhardness in HAZ was significantly decreased. The softening behavior occurs in intermediate critical HAZ and the subcritical HAZ. Song et al. [17] studied the dynamic mechanical properties of 22SiMn2TiB armored steel and revealed a significant difference between dynamic and static mechanical properties. Moreover, the properties measured at different temperatures significantly differ, caused by different phase species. Under stress, the microstructure in different regions (fusion zone (FZ) and HAZ) experienced different behaviors. The microstructure evolution and phase transformation of high-strength 22SiMn2TiB steel during non-isothermal deformation were investigated in detail by Shi et al. [18]. The results indicate that deformation temperature range and amount play a predominant role in phase constitution and volume fraction of the microstructure formed in non-isothermal compressive deformation.

Except that distinctive microstructure and corresponding mechanical properties usually influence failure of LCHS structural components, welding deformation and residual stress also play an essential role. Deng [19] investigated the effects of solid-state phase transformation on the residual stress and the resulting distortion in low-carbon and medium-carbon steels through modeling using ABAQUS simulation software. The results revealed that the solid-state phase transformation does not influence the final residual stress and the welding distortion in low-carbon steel. However, for medium-carbon steel, the final residual stresses and the welding distortion are significantly affected by the martensitic transformation. Mousavi and Miresmaeili [20] studied the effect of different mechanical constraints and shapes of grooved configuration on the residual stresses of welded 304L stainless steel. Some assistance techniques were also used to proceed with post-welding treatment, aiming to optimize the distortion and residual stress of 22SiMn2TiB joints. For instance, Ye [21] successfully used the ultrasonic impact treatment technique to release the residual stress to improve the fatigue performance of the 22SiMn2TiB joint welded by using tungsten inert gas welding. However, these processes have high-cost consumption and low efficiency.

The literature mentioned above shows that the microstructure and mechanical performance at different regions of LCHS weld, distortion, and fundamental component residual stress play a vital role. The elemental composition of the alloy and mutual elemental interactions that occur during welding, together with the combinations of specific welding techniques and strategies (refers to constraint or groove), will have significant and comprehensive influences on the aspects mentioned above. Therefore, the application and development of a designed alloy with low-transformation-temperature (LTT) LCHS wire are necessary and meaningful. An LTT LCHS wire is a welding wire that undergoes a martensitic transformation at low temperatures. The volume expansion from austenite transforming to martensite is used to offset the shrinkage strain caused by the rapid cooling of welding, thereby minimizing or eliminating residual stress. Through designing the LTT wire, the phase content of the post-welding microstructure can not only be regulated to achieve the required mechanical properties but also avoid the drawbacks that are caused by the post-weld treatment as mentioned earlier. However, there needs to be more research on applying LTT LCHS wire on 22SiMn2TiB joint, especially from the perspective of the alloy composition design. Therefore, our current work mainly focuses on two types of welding wires: ER 307Si austenitic stainless steel welding wire commonly used to weld armor steel and the latest designed LTT martensitic mild steel welding wire with adjusted composition, named TX-80. The multiple-pass manual arc welding tests on making the 22SiMn2TiB steel joints using these two wires were carried out, respectively. The resulting microstructure at different regions of the weld was characterized, followed by the analysis and comparison of phase species and content. The

mechanical properties were measured and evaluated, including microhardness, tensile strength, impact strength, distortion, and residual stress. Subsequently, the relationship between these properties and the corresponding microstructure was established. The gaining effect contributed by the modified composition of the improved TX-80 wire compared to the ER 307Si wire was revealed.

2 Experimental methods and setup

In this study, the butt joint test of hot-rolled 22SiMn2TiB steel (base) with the dimension of 320 mm × 150 mm × 12 mm was performed using ER 307Si (feedstock) wire and TX-80 (feedstock) wire, respectively. The diameters of the employed wire were both 1.2 mm. The chemical composition of the used materials is listed in Table 1. The wires were welded with similar welding conditions to make a comparable experiment, as shown in Table 2. The base plates were opened in a V-type groove with a pre-angle position before the welding process, followed by spot welds to fix both ends of the plates. The experimental arrangement can be seen in Fig. 1. The whole groove was completely manually filled by three layers of overlayer welds. After welding each pass, the plate was air-cooled until the top surface was measured at around 80 °C. A Y-groove welding test was carried out in advance to ensure the good anti-crack effect of the newly designed LTT welding wire compared to ER 307Si welding wire during the sequence of welding processes of 22SiMn2TiB steel. The welding conditions are the same as the ones listed in Table 2, and no preheating was carried out. The setup is shown in Fig. 2.

The samples of the welded joint were prepared for metallurgical and mechanical properties investigations. The prepared cross section was cut from the position marked in red dash line, as shown in Fig. 1a, and etched by 2 vol.% Nital (98 vol.% ethanol and 2 vol.% HNO_3) for optical microscopy (Keyence VHX-5000, Osaka, Japan). The tensile samples were prepared according to ASTM E8M-09 standard along the direction vertical to the welding direction, as shown in Fig. 3, and tested at room temperature according to the DIN EN 6892-1 standard employing an Instron-5550 tensile testing machine (Norwood, MA, USA). High-resolution microstructural detailed characterization was carried out using a JEOL FEG-SEM JSM 5600F scanning electron microscope (SEM). Residual stress was measured by the blind-hole drilling method. The measurement principle is to drill a small hole on the material surface to release the stress, leading to strain changes which can be measured with strain gages, and then, the residual stresses were further calculated using the measured strain values. The A-type standardized rosette

Table 2 Reference welding parameters used in this study

Welding parameter	TX-80	ER 307Si
First-layer current/A	125	125
Second-layer current/A	219	220
Third-layer current/A	219	220
First-layer voltage/V	17	15.9
Second-layer voltage/V	22	24.3
Third-layer voltage/V	22	24.3
First-layer wire feed speed/(m min^{-1})	4.1	4.1
Second-layer wire feed speed/(m min^{-1})	7.9	7.9
Third-layer wire feed speed/(m min^{-1})	7.9	7.9
First-layer welding speed/(m min^{-1})	0.21	0.21
Second-layer welding speed/(m min^{-1})	0.19	0.19
Third-layer welding speed/(m min^{-1})	0.16	0.16
Gas flow rate (2% CO_2, 98% Ar)/(L min^{-1})	16	16
Inter-pass temperature/°C	80	80
Pre-setting angle/(°)	3	4

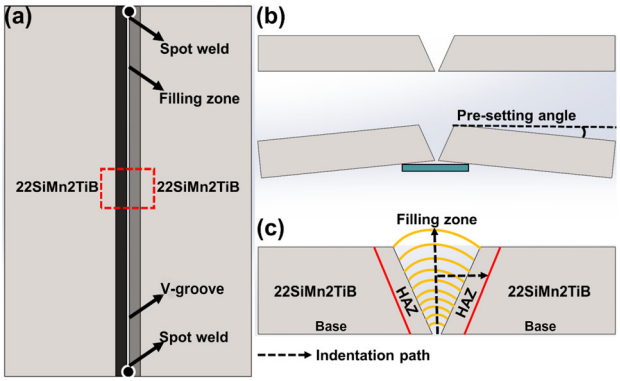

Fig. 1 Experimental setup. **a** Top view; **b** pre-setting angle schematic diagram; **c** side view of cross section

Table 1 Chemical composition of base plate and welding wires (wt.%)

Grade	C	Mn	Si	S	P	Cr	Ni	Mo	Cu	B	Ti	Fe
22SiMn2TiB	0.22	1.7	0.8	0.01	0.01	–	–	–	–	0.002	0.04	Balance
ER 307Si	0.085	7.0	0.85	0.01	0.02	17.7	8.0	0.25	0.25	–	–	Balance
TX-80	0.025	0.7	0.32	0.01	0.01	10	10		0.13	–	–	Balance

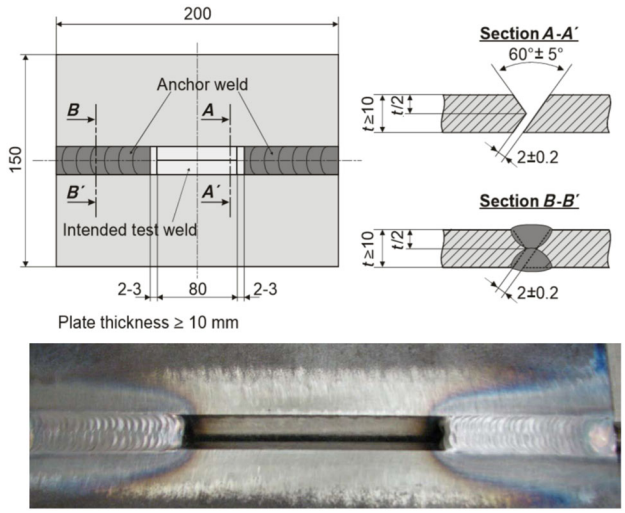

Fig. 2 Schematic drawing and picture of crack test and joint of inclined Y-groove butt

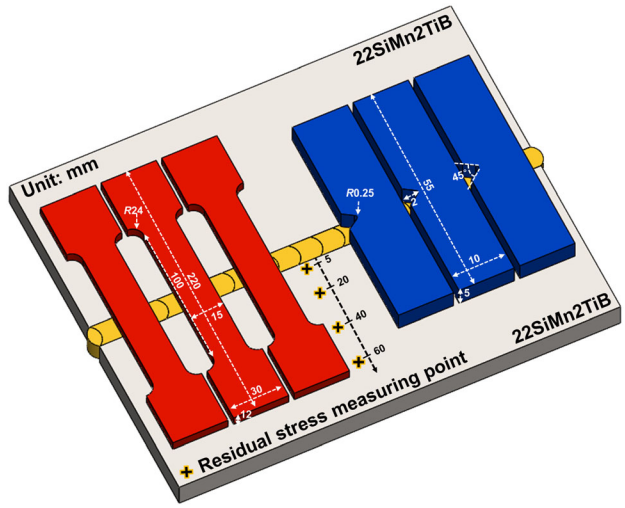

Fig. 3 Schematic diagram of tensile sample location, measured residual stress points, and impact sample location

was used, and the drilling depth was 2 mm. The measuring locations are also schematically shown in Fig. 3.

Aiming to investigate the impact toughness of the welds at room temperature, three impact samples (55 mm × 10 mm × 5 mm) with V-groove notch were cut from the position perpendicular to the welding direction according to the GB/T 2650—2008. JB-300B pendulum impact testing machine was used to perform impact tests on the extracted impact samples. The impact fracture morphology was examined and analyzed by SEM. The measured maximum impact energy absorbed is 150 J, the pendulum moment is 80.38 N m, the pre-elevation angle of the pendulum is 150°, and the distance from the sample center to the pendulum center is 750 mm. In addition, the angle ruler was used to measure the deformation angle, and the Vernier caliper was used to measure the deflection of the two ends of the plate. These two parameters were subsequently adopted to characterize the distortion of the plate. To minimize the error introduced by manual measurement of the angle ruler, the plate distortion was then measured using a Gantry type of three-coordinate measuring machine (Navigator-NCG204015, Maryland, USA) supported by Leader Metrology Inc and the Portable three-coordinate measuring machine (FARO Gage) provided by FARO Technologies, Inc., Orlando, USA. Based on the deflection at both ends of the plate, the distortion can be captured and calculated by the professional 3D image processing software (Geomagic Qualify 2013) supported by Geomagic Inc., North Carolina, USA. Vickers hardness (HV0.1, with 1 N and holding time of 15 s) was measured on a cross section of the weld. One measurement is in the vertical direction from the highest point toward the lowest point, while the other is along the horizontal direction and starts from the middle line of the weld to the base crossing the HAZ. The microhardness test was performed by using a Struers DuraScan-70 machine (Struers Inc., Cleveland, OH, USA), and the indentation path is schematically shown in Fig. 1c.

3 Results and discussion

3.1 Crack resistance test

Figure 4 shows the experimental results of the Y-groove crack resistance test. Traditional ER 100 wire was always employed to weld 22SiMn2TiB steel due to their matched equivalent strengths. However, it can be seen that the hydrogen crack initiated at the weld top and propagated through the entire cross section (Fig. 4a), which was originally caused by the hydrogen pores or hydrides formed during the melt state. The use of ER 307Si austenite welding wire avoids cracking due to the good ability of austenite to dissolve hydrogen (Fig. 4b) instead of the escape or precipitation of hydrogen atoms, nevertheless at the sacrifice of low strength and high cost. As a result, the newly designed TX-80 LTT wire is expected to avoid problems including cracks, strengths, and cost in the meantime during welding, as shown in Fig. 4c.

3.2 Macroscopic inspection

Figure 5 shows the weld appearance of ER 307Si and TX-80 wire on the 22SiMn2TiB steel base. The color chart of the welds with different oxidation levels in Fig. 5b was referred from the American Welding Society Forum (https://app.aws.org/forum/topic_show.pl?tid=19761). The ER 307Si weld intuitively shows a brighter color

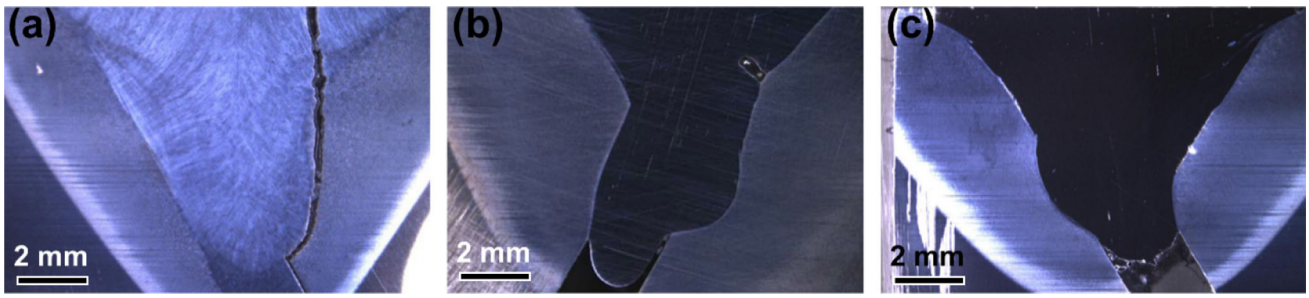

Fig. 4 Results of crack resistance test of welds. **a** ER 100; **b** ER 307Si; **c** TX-80

appearance than the TX-80 weld because slighter oxidation happens in the heating and cooling processes. For steel, except for heat input, chemical composition plays an essential role in the oxidation sensitivity of the weld, such as manganese (Mn), chromium (Cr), and silicon (Si) that are the primary ones. Mn is a mild deoxidant acting as a cleanser taking the sulfur and oxygen out of the melt into the slag. Like Mn, Si is also one of the principal deoxidizers for steel, which can help remove oxygen bubbles from the melt. Besides, ER 307Si welding wire has more Cr than TX-80 welding wire, benefiting an improved oxidation resistance for the weld surface [22].

To investigate the cause of oxidation, the carbon equivalent of the two filler materials was calculated by the IIW-certified carbon equivalent calculation formula, which is 5.4 for ER 307Si welding wire and 2.8 for TX-80 welding wire, respectively. Weld oxidation is a corrosion behavior of oxidizing gas, which can be divided into two aspects: (i) oxidation of melt pool with moisture vapor and oxygen during welding and (ii) oxidation of high-temperature solidified metal in the air. Both result in the formation of oxidation skin on the weld surface, as shown in Fig. 5. Song et al. [23] found that with the increase in carbon equivalent in steel, the oxidation resistance of weld in the air atmosphere decreased. However, Campbell [24] proposed that for low-carbon equivalent or low-carbon steel, the degree of oxidation by water vapor in melt states is more remarkable, so that it can be suppressed by increasing the carbon content. Therefore, it can be inferred that the main period of severe oxidation of TX-80 welds with low-carbon equivalent and carbon content happened in the melting stage. On the contrary, the better anti-oxidation effect of ER 307Si welding wire with high carbon equivalent can be attributed to the rapid cooling rate during the cooling process, which makes the residence time in the high-temperature region very short. Besides, relatively high Si content is also beneficial to increase the carbon equivalent and thus improve the oxidation resistance in melt states, which is reflected in the carbon equivalent formula summarized by Japanese welding institute PCM

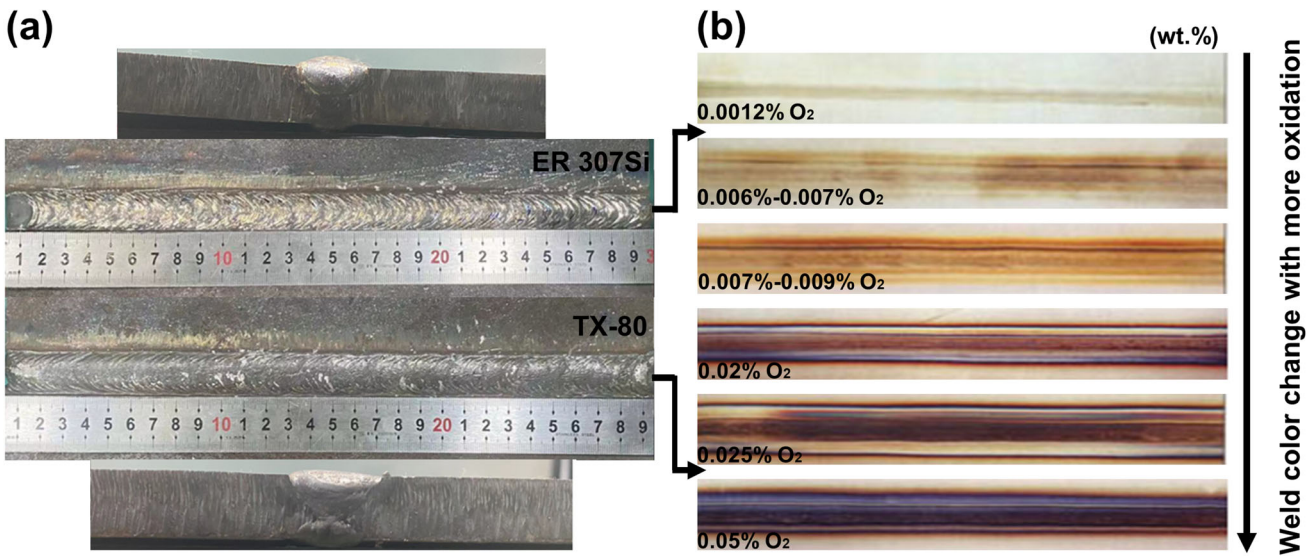

Fig. 5 Weld appearance. **a** Overview of welds; **b** weld color with different oxidation levels

[25] and Düren CEM [26]. It can be concluded that the oxidation of welds mainly comes from the melting period rather than the high-temperature residence period after solidification. For welding the designed TX-80 wire, it is highly recommended to increase the inert gas protection during the welding process or execute in a completely closed inert atmosphere.

In addition, referring to the spatter size and amount surrounding the weld, both kinds of wire experienced a stable welding process, reflected by the continuous and straight weld toe with a smooth transition to the base. However, the wetting angle (the contact angle between the weld toe and base) of ER 307Si wire is relatively larger (closer to 45°), resulting in a higher possibility of weld toe crack than that of TX-80 wire [27]. The equal spacing distance of the "wavy" pattern on the top surface of the weld indicates that the melt flow inside the molten pool is not violent but uniform. This is mainly contributed by the slow welding speed and the short-circuit transition mode of melt droplets adopted in this experiment. Such transition mode was also proved to form less spatter [28], which further promotes better protection of groove sidewalls from eroding caused by other modes like spray transition and global transition. A noticeable difference is that the average width and height of the ER 307Si weld were measured to be 20.12 and 2.31 mm, with aspect ratio of 8.71 while they were 20.53 and 1.82 mm, with aspect ratio of 11.3 for TX-80 weld, respectively. This is attributed to the wettability of the wires containing different additional alloying elements because the species and content of these elements influence the surface tension and fluidity of the melt [29, 30]. Besides, complex physical fluid flow processes are likely to affect the shape of molten bead substantially. It has been concluded from multiple mathematical models that Marangoni convection is the dominant fluid flow force to affect the melt pool [31]. Marangoni forces can operate due to steep temperature gradients inside the melt pool, creating a surface tension gradient. Then, the melt flows from the low- to high-surface tension regions [32]. The JMatPro software calculated and plotted the ER 307Si and TX-80 wire surface tension in Fig. 6a. It shows that the surface tension of both wires is inversely proportional to temperature ($d\sigma/dT$ is negative), meaning that they have the same melt flow pattern, as shown in Fig. 6b. The decrease in surface tension with increase in temperature is due to the fact that with the increase in temperature, the kinetic energy of the molecules increases and hence intermolecular attraction decreases. It can be found that the $d\sigma/dT$ of TX-80 is slightly larger than that of ER 307Si, meaning that the driving force for the metal liquid to flow and spread from the center of the melt pool outwards is greater.

3.3 Distortion and residual stress

In the premise of the base without pre-setting angle, severe deformation occurred for both types of wires after welding; however, the deformation degree of the TX-80 wire is much lower than that of ER 307Si. Angular deflection manual measurement was implemented based on Eq. (1) and Fig. 7 [33], followed by double-check measurement by a Gantry-type three-coordinate measuring machine. According to the average results shown in Fig. 7, it can be found that post-weld deformation for both two wires was significantly improved after the pre-setting angle treatment for the base. The post-weld deformation of the TX-80 wire was mitigated, while that of the ER 307Si was close to the level of the TX-80 wire under the base condition without pre-setting angle. The deflection angles θ of TX-80 and ER 307Si are 2°56′ and 5°32′, respectively, and the vertical deflection distance DZ is 7.68 and 14.46 mm, respectively. Compared with ER 307Si weld without pre-setting angle, TX-80 wire reduces the angular deflection and deflection distance by 47.02% and 46.89%. For the base with pre-setting angle, the angular deflection of the TX-80 sample did not reach the amount of pre-setting angle, which was opposite to the upward warping of the ER 307Si weld plate, and showed a slight downward deflection trend. The DZ of bases with pre-setting angle welded by TX-80 and ER 307Si is −4.1 and 7.41 mm, corresponding to the deflection angles that are −1°34′ and 2°50′, respectively. Compared with the ER 307Si weld with a larger pre-setting angle, the angular deflection and deflection distance of the TX-80 weld with a lower pre-setting angle were reduced by 44.50% and 44.67%.

$$\theta = \arcsin \frac{DZ}{2L} \tag{1}$$

where L is plate width.

The essence of post-weld deformation was the comprehensive effect, including the thermal stresses during welding, the micro-strain caused by the material's phase transformation, the workpiece's constraint conditions, and the release of residual stress after welding. The deformation trend of the base in the three critical stages during the welding process is shown in Fig. 8. Figure 8a shows the initial condition of the undeformed base before welding, and the clamping conditions were almost identical in the case of using TX-80 and ER 307Si. Due to the significant thermal expansion of the weld's upper surface relative to the lower surface, the base metal tended to deform downwards, as shown in Fig. 8b. Once the welding was completed, the base began to cool, which allowed the molten metal to shrink, causing the two side ends of the base to tend to deform upwards (Fig. 8c). Due to the constraint at both ends, the deformation was limited, and a

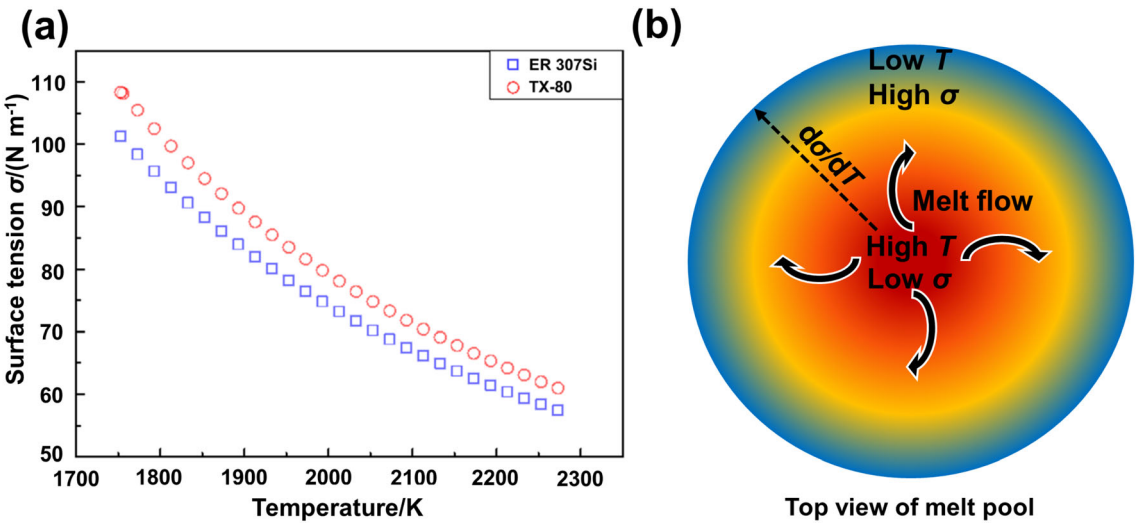

Fig. 6 Thermophysical properties of TX-80 and ER 307Si. **a** Surface tension change with temperature; **b** schematic diagram of melt flow. *T*—Real temperature at different positions of melt pool

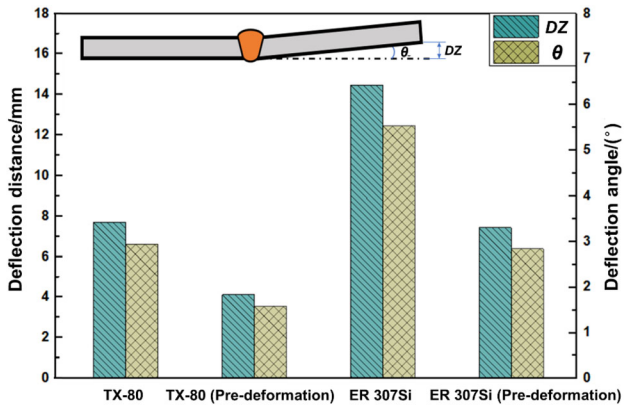

Fig. 7 Angular deflection angle and vertical deflection distance for TX-80 and ER 307Si wires

corresponding tensile stress was generated inside the weld. However, for TX-80 LTT wire, when the cooling temperature reached a lower temperature, it would undergo a martensitic transformation, contributing to a macro volume expansion due to the lattice size difference between the face-centered cubic (FCC) and body-centered cubic (BCC) lattice structures, as shown in Figs. 8d and 9. Such volume expansion can offset or even exceed the shrinkage during the early cooling stage, leading to a downward deformation at both ends of the base. When the constraint was released, the previously formed residual stress higher than the base's yield strength forced the plate to undergo further plastic deformation, reflected in the aforementioned angular deformation, until a structurally sustainable stress balance state was reached.

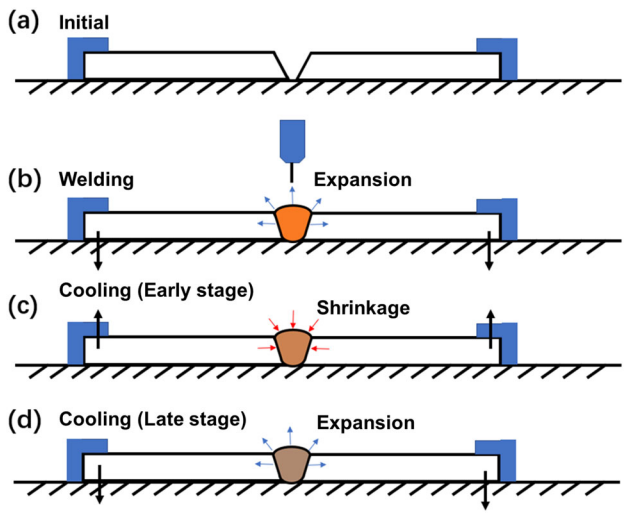

Fig. 8 Schematic diagram of welding distortion evolution. **a** Initial stage; **b** heating stage; **c** early cooling stage; **d** late cooling stage

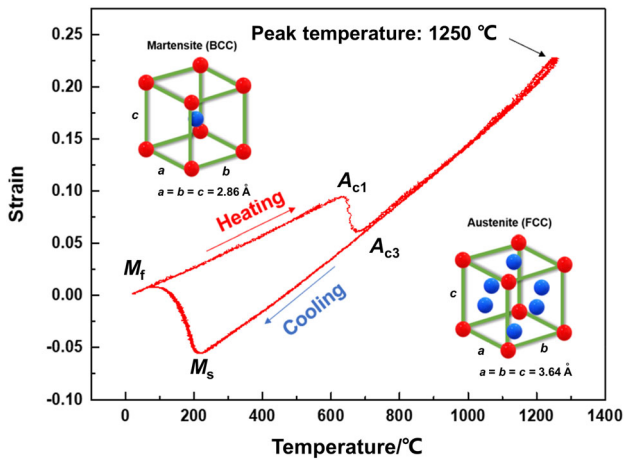

Fig. 9 Thermal expansion of TX-80 wire measured by Gleeble thermal–mechanical simulator

Residual stress was measured on the samples treated with pre-setting angles through the hole drilling test. The residual stress measurement points were perpendicular to the weld with the distances from the fusion line of 5, 20, 40, and 60 mm, respectively, as schematically shown in Fig. 3. Figure 10 shows the measurements of the samples welded using TX-80 and ER 307Si welding wires. In both cases, the Von Mises residual stress, which combines the three principal stresses into an equivalent stress, first decreased and then increased with the distance increasing from the weld toe (Fig. 10a). The maximum values are located in the HAZ.

Moreover, the maximum Mises stress value of ER 307Si (782.4 MPa) is much higher than that of TX-80 (497.5 MPa), which is much closer to the yield strength of the base. This is due to the aforementioned martensitic transformation in the TX-80 LTT wire, in which case the expansion volume caused by phase transformation far exceeds the shrinkage of welding cooling, so that compressive stress was formed to offset partial tensile residual stress. However, ER 307Si did not experience martensitic transformation, leading to the residual stress at the weld still remaining to be tensile states. This means that the LTT material can reduce the residual tensile stress of the weld to a certain extent, which is beneficial to improving the mechanical properties of the joint. For the residual stress distribution perpendicular to the welds, both TX-80 and ER 307Si change from tensile stress (gradually decreasing) to compressive stress (gradually rising), but obviously TX-80 has a faster stress changing rate compared to ER 307Si, and the value of compressive stress is much larger than that of ER 307Si. In the TX-80 sample, the residual compressive stress perpendicular to the weld at two points 40 and 60 mm from the weld fusion line exceeds the residual stress parallel to the weld and becomes the largest contributor to the welding residual stress at this point. This means that high compressive residual stress exists in the base region far from the HAZ. This effectively helps to hinder crack propagation which can help to improve the fatigue properties of the weld [34].

3.4 Microstructure and microhardness distribution

Figure 11 shows the hardness distribution of TX-80 and ER 307Si weld cross sections. Distinct weld zone (FZ), coarse-grained heat-affected zone (CGHAZ), fine-grained heat-affected zone (FGHAZ), critical heat-affected zone (ICHAZ), subcritical heat-affected zone (SCHAZ), and base metal (BM) were displayed in the map with the hardness distribution profile covering the map as well. After the uniform etching of TX-80 LTT and the ER 370Si welds, the weld and base metal color is quite different, and the boundary between the weld and the HAZ is visible to the naked eye. This is due to the addition of high content of Cr and Ni elements in the TX-80 wire, which significantly improves the corrosion resistance of the weld. In addition, there still exists a slight difference between the two cross sections, revealed by the formation of the first layer on the back of the base and especially the shape and size of each sub-HAZ zones. This was resulting from the heat input fluctuation caused by the manual welding process and the pre-setting angle differences, despite the same parameters being set up in the comparison experiment.

It is well known that for ordinary stainless steel with different $w_{\text{Cr-eq}}/w_{\text{Ni-eq}}$ [35], four different solidification modes are available, including ferrite, ferrite–austenite, austenite–ferrite mode, and austenite mode, where w_i

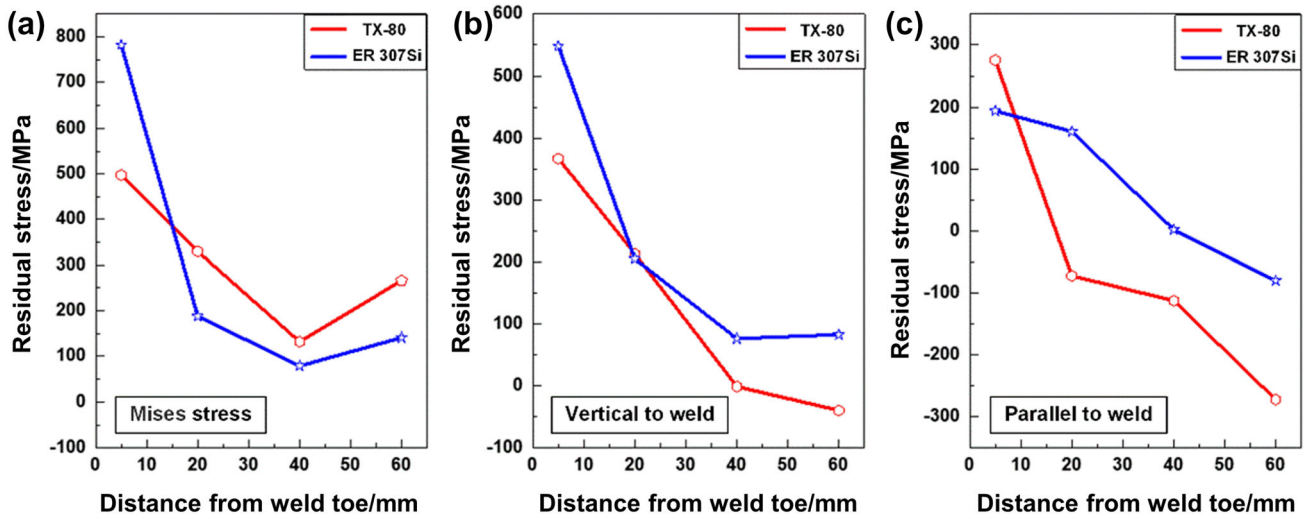

Fig. 10 Residual stress distribution of welds using TX-80 and ER 307Si wires. **a** Mises stress; **b** vertical to weld; **c** parallel to weld

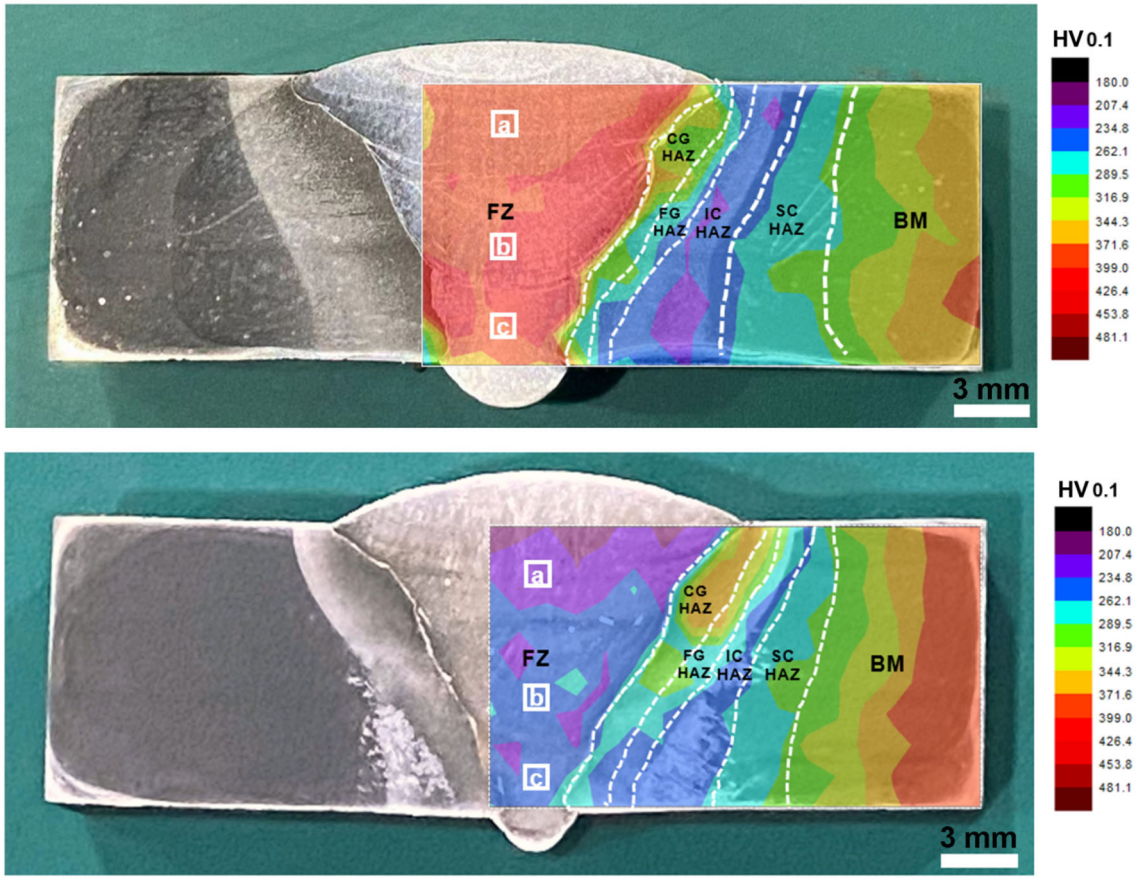

Fig. 11 Hardness distribution of weld cross section. **a** TX-80; **b** ER 307Si

means the weight percent of alloying element i and eq is the equivalent weight percent. Therefore, the multi-element system in stainless steels is generally simplified to Fe–Cr–Ni ternary system to obtain easier the solidification modes, phase species, and content at a specific condition. According to Schaeffler formula in Fig. 12 [36] ($w_{\text{Cr-eq}} = 1\%w_{\text{Cr}} + 1\%w_{\text{Mo}} + 1.5\%w_{\text{Si}} + 0.5\%w_{\text{Nb}}$, $w_{\text{Ni-eq}} = 1\%w_{\text{Ni}} + 30\%w_{\text{C}} + 0.5\%w_{\text{Mn}}$), the $w_{\text{Cr-eq}}/w_{\text{Ni-eq}}$ of TX-80 and ER 307Si welds can be figured out and marked with red and blue circles separately. It can be seen that the microstructure of TX-80 weld at room temperature is dominated by martensite, while that of ER 307Si weld mainly consists of austenite. Since the blue point representing ER 307Si is located in zone A (austenite) but close to zone A + F (ferrite), non-equilibrium solidification is highly possible to occur to form ferrite. In addition, the red point representing TX-80 is located at the junction of zone A + M (martensite) and zone M, which may produce residual austenite in the final microstructure.

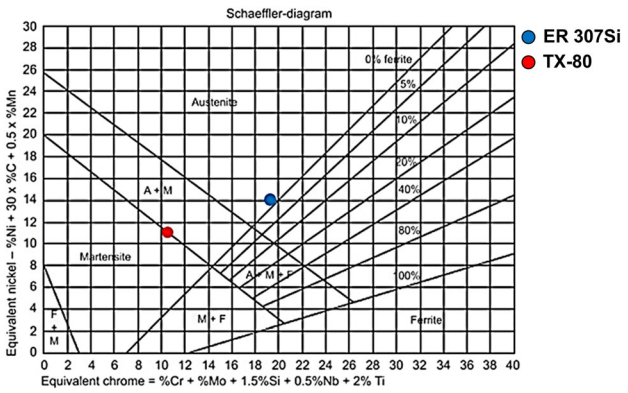

Fig. 12 Constitution diagram for stainless steel

The microstructure of the weld zone and HAZ of TX-80 and ER 307Si wires were characterized and shown in Figs. 13 and 14. Since the welding condition was almost the same, the HAZ at the base experienced the same thermal history, from which it can be inferred that the microstructure change was similar. The microstructure at the weld zone of TX-80 LTT wire was mainly composed of lath martensite and a small amount of retained austenite, as shown in Fig. 13. For TX-80 weld, the solidification mode is mainly austenite mode. During the welding cooling period, when the temperature drops and is lower to the liquidus temperature (L + γ region), the liquid phase begins to precipitate austenite until completing the entire

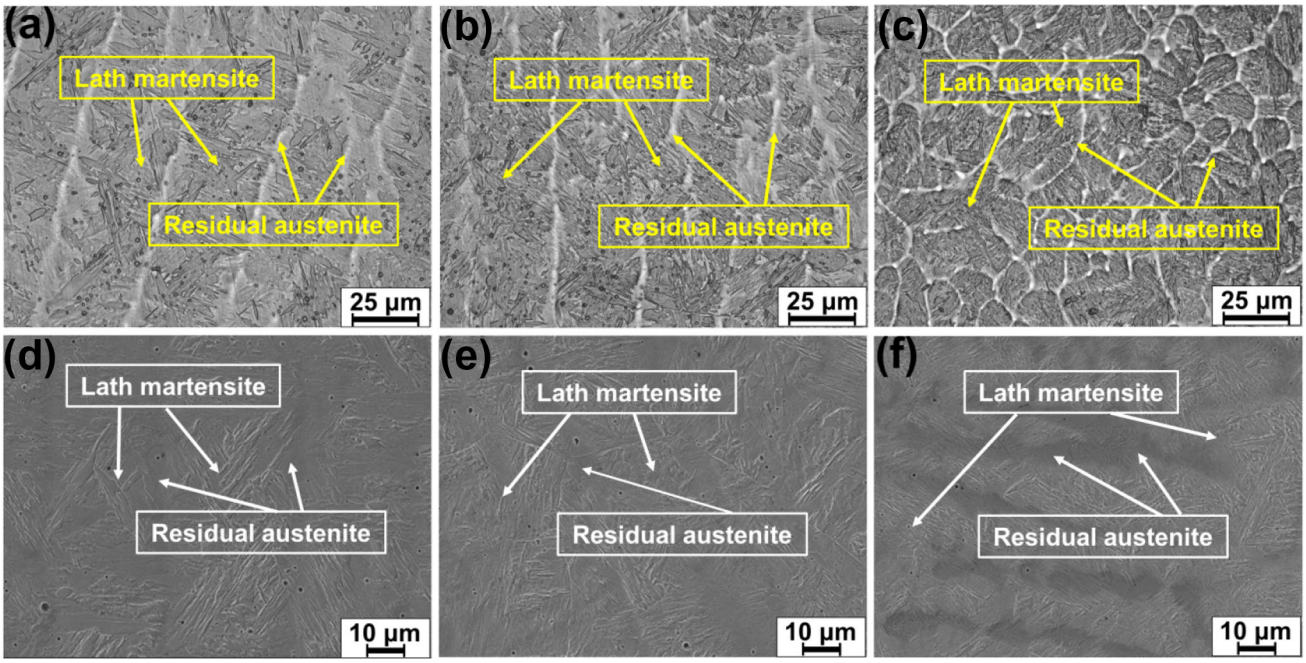

Fig. 13 Microstructure at TX-80 weld zone. **a**, **d** Top region; **b**, **e** middle region; **c**, **f** bottom region

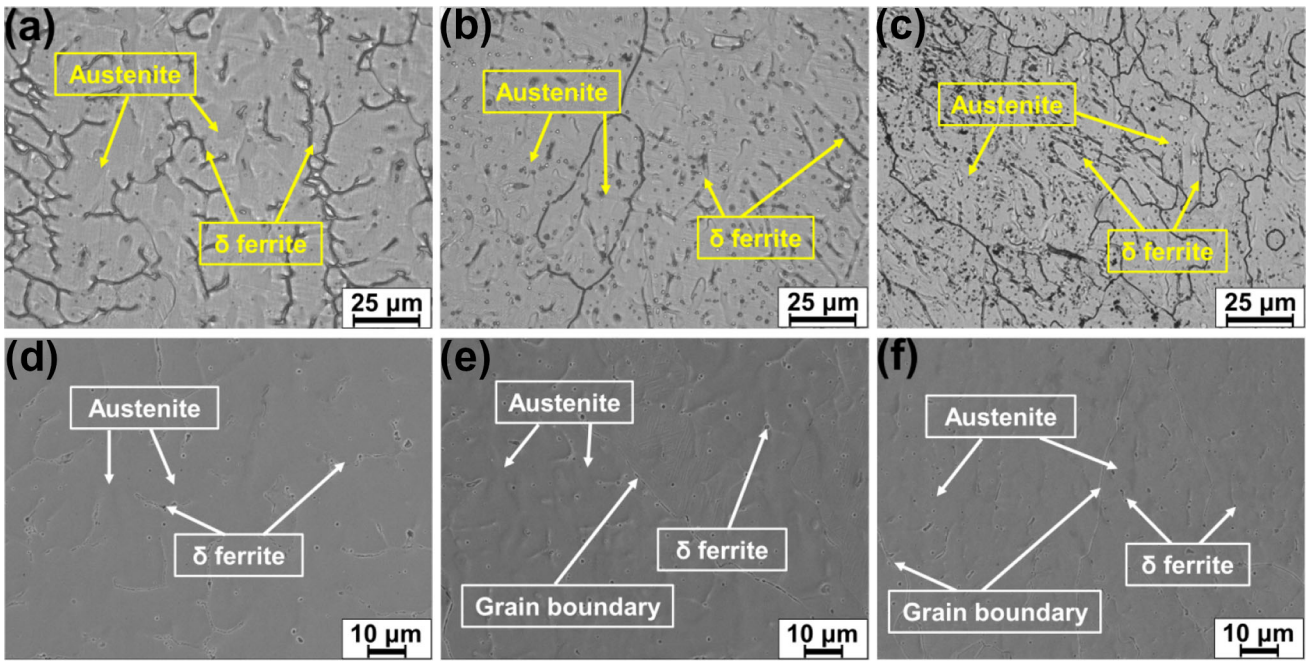

Fig. 14 Microstructure at ER 307Si weld zone. **a**, **d** Top region; **b**, **e** middle region; **c**, **f** bottom region

austenitization (L → γ). Austenite begins martensitic transformation after reaching M_s temperature (γ → M) in the subsequent cooling to room temperature. Due to the influence of solute elemental content and segregation caused by rapid solidification on M_s and M_f temperatures, austenite has residue in the end. The martensite structure was composed of a large number of lath martensite mixed, while the retained austenite structure with the shape of white layers was located between the lath martensite. It should be noted that the bulk martensitic growing is not confined by newly formed martensite cell boundaries but intersect freely. As suggested in a previous study [37], the compositional gradient does not interfere with the development of martensite block, so that the structure continuity was not interrupted by the unit martensite cell boundaries.

The solidification of ER 307Si weld is mainly austenite + ferrite. The solidification process contains two stages: (i) Liquid–solid transition. The liquid metal cools to L + A dual phase region and begins to form austenite grains. As cooling progressed, constitutional undercooling at the local region promotes the occurrence of high-temperature eutectic reaction $L \rightarrow \gamma + \delta$ until the melt is completely solidified [38]. (ii) Solid-phase transformation. The previously formed δ dissolved as cooling progressed, so that austenite single-phase region was obtained at room temperature. Because the melt pool is in a non-equilibrium state under the large temperature gradient, the transformation of each solid phase is incomplete. At the same time, the ultra-fast cooling rate is also an essential factor in influencing phase transformation during solidification, resulting in the coexistence of austenite and potential δ-ferrite at room temperature. Therefore, the microstructure at the weld zone of ER 307Si wire was mainly composed of an austenite matrix and a black skeleton-like ferrite phase, as shown in Fig. 14. It can be seen that both sides of the two welds have columnar grain structures, while the center of the welds shows equiaxed grain structures, which is related to the directional growth of grains along the direction of heat flow. Additionally, as the welding layer increases, the grains become larger and larger due to the heat accumulation effect [39].

The profile of the weld zone corresponds well with the hardness distribution. The welding process causes the formation of complex and non-uniform microstructures in different regions, as shown in Fig. 15, resulting in mechanical properties with a severe difference from the base. The CGHAZ was adjacent to the fusion zone and is approximately 1.5 to 3 mm wide. The material here was heated to a temperature much higher than A_{c3}, so that uniform austenite was formed. Due to the relatively fast heating rate of around 500 °C/s [40], the transformation starts between A_{c1}–800 °C and ends around A_{c3} (∼950 °C). The peak temperature at CGHAZ is above 1100 °C. Therefore, the austenite grains start to grow exponentially, so that the grain size here can be several times larger than the base material.

In addition, with a high cooling rate near the FZ, a hard martensitic microstructure and retained austenite are formed in a short cooling period, leading to a higher hardness (270–380 HV) in this area. Therefore, in many cases, the toughness in the CGHAZ area is the lowest in the weld structure. The distance between the FGHAZ and the centerline of the weld is about 1.5 to 5 mm. The peak temperature in this region is higher than A_{c1}. Owing to the same phase transition, the phases are similar to that of CGHAZ, but the microstructure grain size is uniform and finer due to the shorter peak temperature dwelling time. However, because of the slow cooling rate, high content of retained

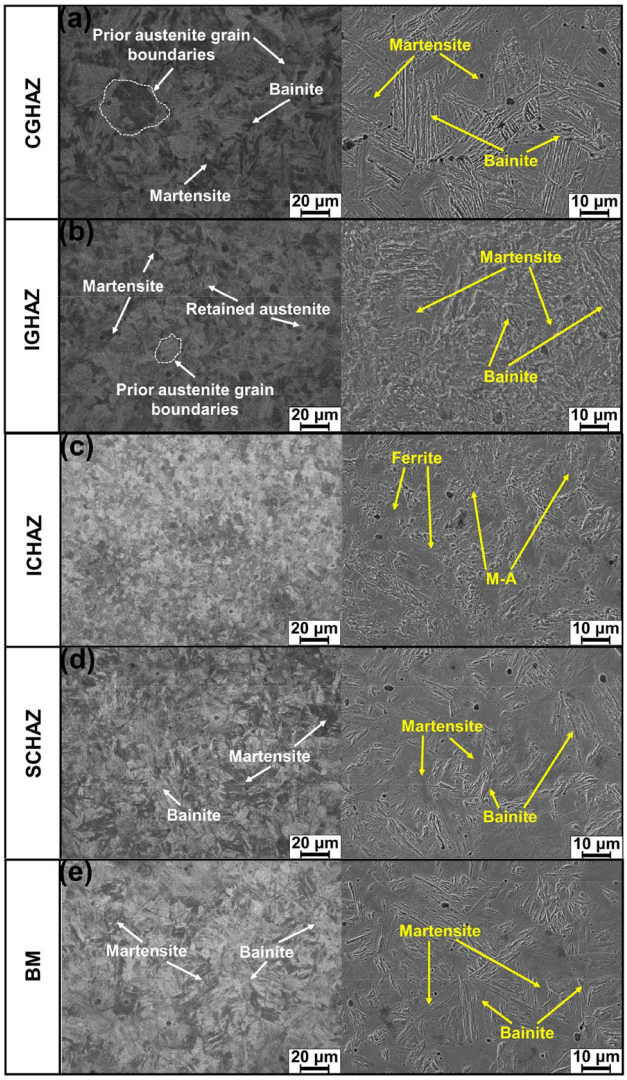

Fig. 15 Microstructure of sub-HAZ. **a** CGHAZ; **b** IGHAZ; **c** ICHAZ; **d** SGHAZ; **e** BM

austenite existed here, causing the hardness reduction. The distance between the ICHAZ and the weld centerline is about 5 to 8 mm. The peak temperature in this region was between A_{c1} and A_{c3}, indicating that the incomplete austenite transformation promoted an inhomogeneous microstructure distribution. Because austenite has a higher ability to dissolve carbon in this temperature range, the carbon content of the austenitized part further increases because the region stayed in this critical range for a more extended period due to a relatively slow cooling rate. During cooling, the austenite transformed into ferrite that was softer than the base material, while the carbon content of the non-austenitized parts was further reduced. The local welding temperature exceeded the tempering temperature, decreasing hardness significantly (220–270 HV), indicating that a typical softening zone is usually considered the weakest section of a weld. Therefore, ICHAZ consists of tempered

martensite, retained austenite, and ferrite. Tempered martensite is distributed along the grain boundaries, and ferrite is distributed in the grain center. Due to the decomposition of martensite, tempered martensite was formed with the precipitation of carbides and the recrystallization of martensite. As the distance from the SCHAZ further increased to the base material, the tempering temperature gradually decreased. Tempered martensite was the majority in the region. The hardness gradually increased and finally approached the hardness of the base material, which was composed of continuous martensite distributed along grain boundaries and surrounding martensite islands.

3.5 Tensile strength and impact toughness

The strain–stress curve of the TX-80 and ER 307Si welds is shown in Fig. 16a. The ER 307Si sample was broken at the center of the weld, while the fracture position of the TX-80 sample is in the FGHAZ softening zone that distributed with inhomogeneous microstructure and located in the transition from the HAZ to the base material. The elongation of TX-80 and the ER 307Si tensile samples is 6.76% and 6.01%, respectively. In contrast, the ultimate tensile strengths (UTS) of welds are 877 and 667 MPa, respectively, which is consistent with the microhardness measurements at the corresponding fracture zone. According to the empirical formula between hardness and strength [41], the UTS in different regions of welds can also be estimated, as shown in Fig. 17. In general, tensile fracture often occurs if the weld has a softening zone. This is because the microstructure of the softening zone is tempered martensite and austenite, and its hardness is lower than that of other areas in the weld. Under uniaxial tensile stress, the microstructure in the softening zone is more prone to plastic deformation and necking until the final fracture.

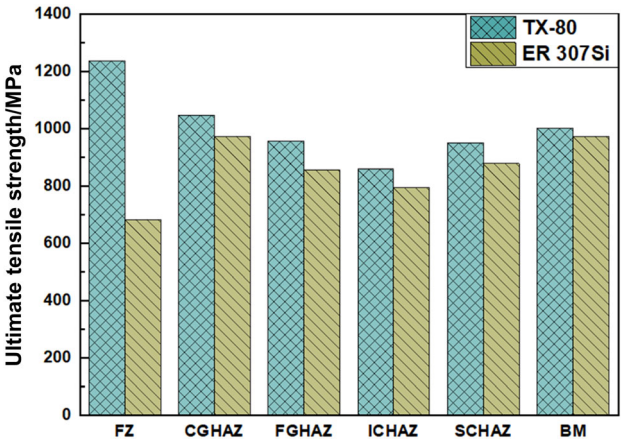

Fig. 17 Predicted UTS in different regions of welds

The impact toughness of the TX-80 and ER 307Si welds is shown in Fig. 16b. It can be seen that the average impact toughness of the ER 307Si weld is 143.9 J/cm^2, much higher than that of the TX-80 weld, which is only 36.7 J/cm^2. The macro photograph of the impact sample is shown in Fig. 16b as well. The ER 307Si sample is covered with sharp tearing edges, and the entire fracture has only the fiber area and shear lip, revealing a pretty high-impact toughness. In addition, a small radiation zone appeared at the bottom half zone of the TX-80 impact sample. The shear lip is also slightly smaller than that of ER 307Si sample. Although there are some tearing edges, the amount is small, and the tip is not sharp. The sign of the radiation zone is more pronounced, but the proportion of the fiber zone and the shear lip is much more reduced, indicating that its toughness is relatively poor. From the

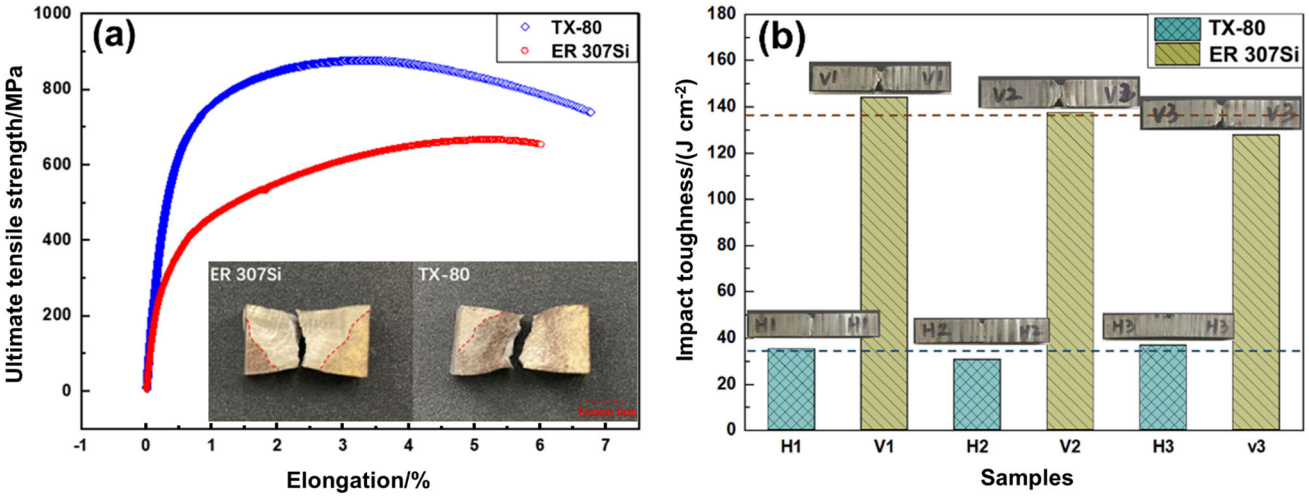

Fig. 16 Mechanical properties of TX-80 and ER 307Si welds. **a** Strain–stress curve; **b** impact strength

microstructure point of view, the leading cause for such a significant impact toughness difference is that the microstructure at the TX-80 weld is mainly composed of martensite and a small amount of retained austenite. Martensite has high strength and hardness but insufficient toughness, showing poor impact toughness. The microstructure of ER 307Si weld is composed of a large amount of austenite and part of skeleton ferrite. Both austenite and ferrite have good toughness, so that the impact absorption energy of the weld is relatively high.

3.6 Fractography

The microscopic graphs of the fracture after the tensile test are shown in Fig. 18a and b. Large cracks were observed on the fracture surface of both TX-80 and ER 307Si samples, which is the main reason for the low elongation of the two samples. A zoomed-in view of the TX-80 fracture sample shows deep dimples of varying size, shallow dimples distributed between deep dimples, and shear lips. The presence of deep dimples is usually associated with stress concentration. As mentioned previously, the microstructure has experienced excessive tempering at the softening zone, which can easily promote large carbides precipitation [42]. The coarse particles of these carbides are brittle and generally regarded as the crack initiation site to induce large stress concentrations. A cleavage feature appeared at the sample surface, and the massive dimples showed the combination of ductile and brittle fracture modes of the TX-80 and ER 307Si joint. However, the brittleness of ER 307Si weld is greater, revealed by the reduced depth of fracture dimples and tinier pores, which were the main factors causing large cracks generation and relatively lower elongation.

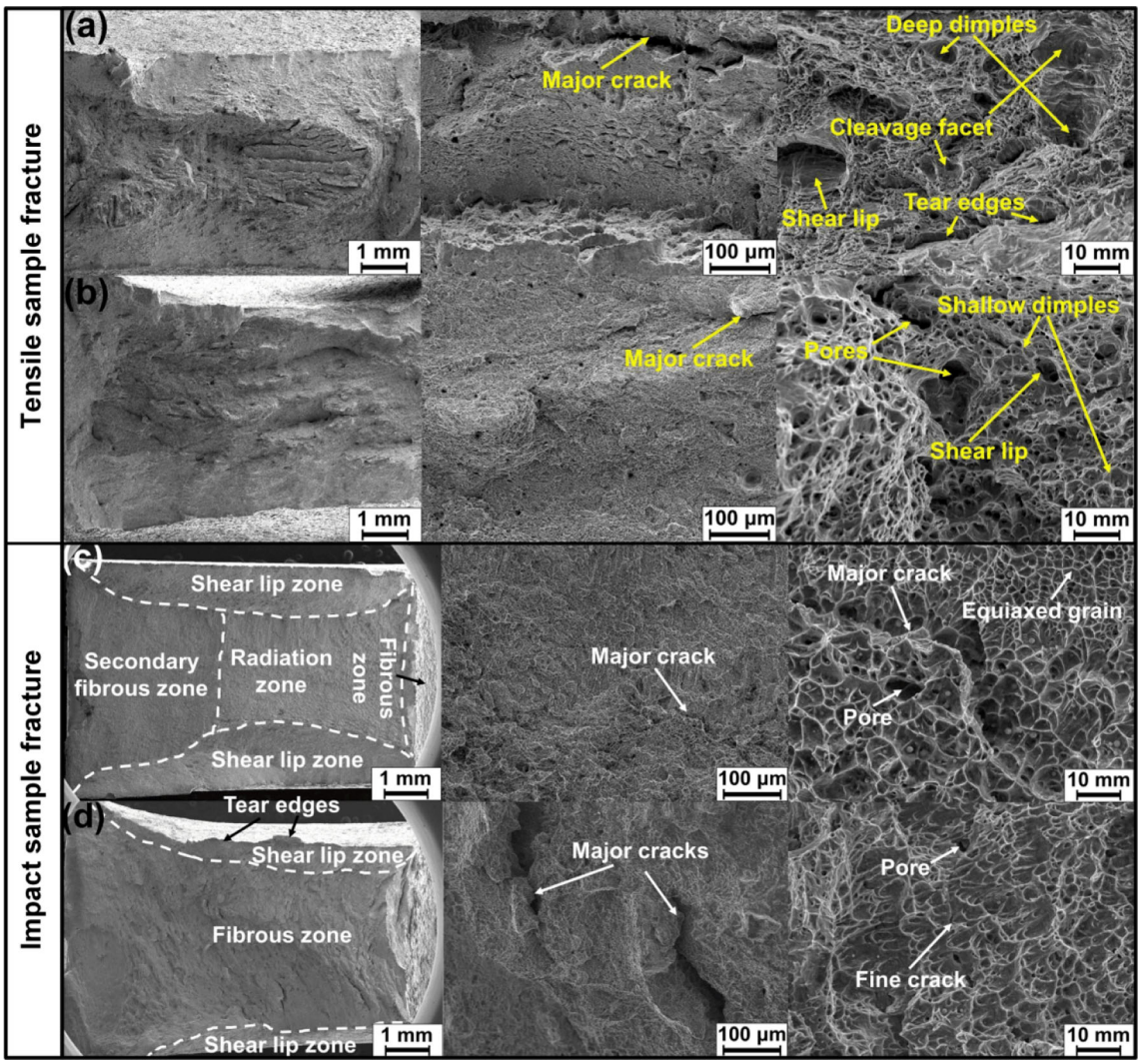

Fig. 18 Fracture morphology. **a** Tensile fracture of TX-80 weld; **b** tensile fracture of ER 307Si weld; **c** impact fracture of TX-80 weld; **d** impact fracture of ER 307Si weld

The microscopic graphs of the fracture after the impact test are shown in Fig. 18c and d. It can be seen that the uneven fracture surface of ER 307Si sample is covered with sharp tearing edges. The shear lip and the fiber region are significant, indicating a high-impact toughness. However, only a few smooth tearing edges are found on the TX-80 fracture surface. A larger radiation zone at the lower region of the fracture surface and more giant shear lips than those of ER 307Si sample indicate the relatively poor toughness, which can also be shown by the reduced fiber area and shear lips.

4 Conclusions

1. There will be deformation when welding the bases with and without pre-setting angle. However, the deformation of the TX-80 weld is much smaller than that of the ER 307Si weld.
2. The Von Mises residual stress of TX-80 and ER 307Si weld first decreased and then increased with increased distance from the weld toe. The maximum residual stresses are located in the HAZ, but the residual stress of ER 307Si is much higher than that of TX-80, which is close to the yield strength of the base.
3. The microstructure at the TX-80 weld is mainly composed of martensite and a small amount of retained austenite. In contrast, the microstructure of the ER 307Si weld consists of a large amount of austenite and a minority of skeleton-like ferrite.
4. The microhardness of TX-80 and ER 307Si welds showed a distribution trend of initial increase and then decrease from the weld to both sides of the base material. The microhardness at the TX-80 FZ reaches 432 HV, which is higher than that of the ER 307Si (around 230 HV) and base (around 400 HV), but there exists a softening zone with smaller microhardness in HAZ.
5. The elongation of TX-80 and the ER 307Si tensile samples is 6.76% and 6.01%, while the ultimate tensile strengths are 877 and 667 MPa, respectively. The average impact toughness of the ER 307Si weld is 143.9 J/cm^2, much higher than that of the TX-80 weld, which is only 36.7 J/cm^2. Different phase compositions and ratios mainly contribute to the differences.
6. The fracture position is located in the softening zone for the TX-80 weld and at the ER 307Si weld center.

Acknowledgements The work is sponsored by the National Key Laboratory Foundation of Science and Technology on Materials under Shock and Impact (2021ZX52002222019), National Natural Science Foundation of China (NSFC No. U2141216), and the Beijing Institute of Technology Young Scholar Startup Program. The authors gratefully acknowledge financial support from the China Scholarship Council (CSC No: 202106030118) and technical support from the Experimental Center of Advanced Materials (ECAM) of the Beijing Institute of Technology.

Declarations

Conflict of interest The authors declare no competing financial interest.

References

[1] W.M.J.J. Garrison, JOM 42 (1990) No. 5, 20–24.
[2] T.W. Montemarano, B.P. Sack, J.P. Gudas, M.G. Vassilaros, H.H. Vanderveldt, J. Ship Prod. 2 (1986) 145–162.
[3] Y.K. Wang, J.A. Wharton, R.A. Shenoi, Corros. Sci. 86 (2014) 42–60.
[4] Z.D. Lin, Wire and arc additive manufacturing of thin structures using metal-cored wire consumables: microstructure, mechanical properties, and experiment-based thermal model, Delft University of Technology, Delft, Holland, 2019.
[5] K. Song, Z. Lin, Z. Zhu, X. Zhao, W. Ya, C. Goulas, Y. Li, X. Yu, J. Mater. Sci. 58 (2023) 13183–13204.
[6] L. Qi, L. Yang, H.E. Shao-Hua, Bus Coach Technol. Res. 74 (2012) 375–391.
[7] J. Xu, Y. Peng, S. Guo, Q. Zhou, J. Zhu, X. Li, J. Mater. Eng. Perform. 28 (2019) 6669–6681.
[8] Y. Wang, K. Zhang, Z. Guo, N. Chen, Y. Rong, Mater. Sci. Eng. A 552 (2012) 288–294.
[9] A. Barcellona, D. Palmeri, Metall. Mater. Trans. A 40 (2009) 1160–1174.
[10] B. Beidokhti, A. Dolati, A. Koukabi, Mater. Sci. Eng. A 507 (2009) 167–173.
[11] S. Papaefthymiou, A. Vazdirvanidis, G. Pantazopoulos, C. Goulas, J. Fail. Anal. Prev. 17 (2017) 79–85.
[12] X. Yu, J.L. Caron, S.S. Babu, J.C. Lippold, D. Isheim, D.N. Seidman, Acta Mater. 58 (2010) 5596–5609.
[13] T. Mohandas, G. Madhusudan Reddy, B. Satish Kumar, J. Mater. Process. Technol. 88 (1999) 284–294.
[14] C. Pandey, M.M. Mahapatra, P. Kumar, N. Saini, Mater. Sci. Eng. A 712 (2018) 720–737.
[15] P.H.O.M. Alves, M.S.F. Lima, D. Raabe, H.R.Z. Sandim, J. Mater. Process. Technol. 252 (2018) 498–510.
[16] M. Tamizi, M. Pouranvari, M. Movahedi, Sci. Technol. Weld. Join. 22 (2017) 327–335.
[17] K. Song, Z. Lin, Y. Fa, X. Zhao, Z. Zhu, W. Ya, Z. Sun, X. Yu, Metals 13 (2023) 764.
[18] Z. Shi, K. Liu, M. Wang, J. Shi, H. Dong, J. Pu, B. Chi, Y. Zhang, L. Jian, Mater. Sci. Eng. A 535 (2012) 290–296.
[19] D. Deng, Mater. Des. 30 (2009) 359–366.
[20] S.A. Mousavi, R. Miresmaeili, J. Mater. Process. Technol. 208 (2008) 383–394.
[21] X. Ye, J. Mech. Eng. 45 (2009) 283–286.
[22] Y. Yang, A. Wang, D. Xiong, Z. Wang, D. Zhou, S. Li, H. Zhang, Surf. Coat. Technol. 384 (2020) 125316.
[23] L. Song, Y. Peng, H. Zhao, Y. Cao, Q.J. Fang, Front. Mater. 9 (2022) 957669.
[24] J. Campbell, Complete casting handbook: metal casting processes, metallurgy, techniques and design, Butterworth-Heinemann, Oxford, UK, 2011.
[25] H. Kihara, T. Kanazawa, H. Tamura, P. Roy Soc. A-Math. Phy. (1976) 247–258.

[26] M. Alhassan, Y. Bashiru, World J. Eng. Technol. 9 (2021) 782–792.
[27] T. Nykänen, G. Marquis, T. Björk, Effect of weld geometry on the fatigue strength of fillet welded cruciform joints, in: Proceedings of the International Symposium on Integrated Design and Manufacturing of Welded Structures, Lappeenranta University of Technology, Lappeenranta, Lake Saimaa, Finland, 2007.
[28] S.J. Bless, J. Phys. D. Appl. Phys. 7 (1974) 526.
[29] Q.D. Wang, Y.Z. Lu, X.Q. Lu, L. Yizhen, X.Q. Zeng, W.J. Ding, Y.P. Zhu, Q.H. Li, J. Lan, Mater. Sci. Eng. A 271 (1999) 109–115.
[30] B. Keene, Int. Mater. Reviews (1988) 1–37.
[31] K.C. Mills, B.J. Keene, Int. Mater. Rev. 35 (1990) 185–216.
[32] C.B. Kim, D.W. Janes, S.X. Zhou, A.R. Dulaney, C.J. Ellison, Chemistry of Materials 27 (2015) 4538–4545.
[33] R. Ghorbel, A. Ktari, N. Haddar, Int. J. Adv. Manuf. Technol. 113 (2021) 3525–3542.
[34] G. Pouget, A.P. Reynolds, Int. J. Fatigue 30 (2008) 463–472.
[35] M. Lervåg, C. Sørensen, A. Robertstad, B.M. Brønstad, B. Nyhus, M. Eriksson, R. Aune, X. Ren, O.M. Akselsen, I. Bunaziv, Metals 10 (2020) 272.
[36] A.L. Schaeffler, Met. Progress 56 (1949) 680.
[37] C.R. Shamantha, R. Narayanan, K.J.L. Iyer, V.M. Radhakrishnan, S.K. Seshadri, S. Sundararajan, S. Sundaresan, Mater. Sci. Eng. A 287 (2000) 43–51.
[38] C. Chen, T.T. Feng, G.R. Sun, H.J. Zhang, Manuf. Lett. 33 (2022) 42–45.
[39] Z.D. Lin, K.J. Song, B.D. Castri, W. Ya, X.H. Yu, J. Alloy. Compd. 921 (2022) 165630.
[40] R.C. Reed, H.K.D.H. Bhadeshia, Acta Metall. Mater. 42 (1994) 3663–3678.
[41] Z. Lin, K. Song, W. Ya, X. Yu, Journal of Physics: Conference Series 2101 (2021) 012049.
[42] W. Liu, X. Liu, F. Lu, X. Tang, H. Cui, Y. Gao, Mater. Sci. Eng. A 644 (2015) 337–346.